ADVANCED FUNCTIONAL MATERIALS
www.afm-journal.de

Composition and Resulting Band Alignment at the TiO_2/InP Heterointerface: A Fundamental Study Combining Photoemission Spectroscopy and Theory

*Mohammad Amin Zare Pour, Muhammad Nawaz Qaisrani, Christian Höhn, Johannes Laurenz Wolf, Negin Mogharehabed, Jennifer Velazquez Rojas, Wolfram Jaegermann, Erich Runge, Roel van de Krol, Thomas Hannappel, Christian Dreßler, and Agnieszka Paszuk**

The composition and resulting band alignment at the TiO_2/InP heterointerface are critical for optimizing semiconductor-based photoelectrochemical and photovoltaic devices. Hence, a systematic investigation of the chemical composition and electronic properties of TiO_2 film grown via atomic layer deposition (ALD) on p-doped, atomically well-ordered, phosphorus-terminated InP(100) surfaces is conducted. A combination of UV and X-ray photoelectron spectroscopy with ab initio molecular dynamics simulations is applied to provide a comprehensive atomic-scale understanding of the heterointerface. These results reveal that the P—P dimers in the first monolayer remain intact during the initial ALD cycles, while oxygen preferentially binds between indium in the second monolayer and phosphorus in the first monolayer, leading to the formation of interfacial indium phosphate ($InPO_x$) species. The presence of chlorine residues from the $TiCl_4$ precursor persists throughout the deposition process and influences the chemical environment of the interface. Band alignment analysis confirms the formation of a type-II heterojunction, characterized by a valence band offset of approximately 2.3 eV and a conduction band offset of 0.45 eV, facilitating charge carrier separation essential for high-efficiency photoelectrochemical applications. These detailed insights into the interfacial chemistry and electronic structure are fundamental to advance the development of efficient semiconductor-based energy conversion devices.

1. Introduction

In artificial photosynthesis, sunlight is directly converted into chemical fuels such as hydrogen (H_2). Currently, the majority of H_2 is still produced from fossil fuels. A sustainable alternative is photoelectrochemical (PEC) water splitting, which enables direct solar-driven hydrogen production without carbon dioxide emissions. Compared to photovoltaic (PV)-powered electrolysis, PEC devices offer advantages such as the possibility to use Earth-abundant catalysts due to much (20–100x) lower current densities, and improved thermal management, which enhances electrochemical reaction kinetics.[1] Despite these benefits, a major challenge remains: the generation of sufficient photovoltage to drive water splitting while maintaining the stability of the device under operation. While some oxide-based wide-bandgap photoabsorbers provide the necessary photovoltage, they absorb only UV light, significantly limiting the achievable efficiency.[2,3] In contrast, III-V semiconductors offer tunable

M. A. Zare Pour, T. Hannappel
Fundamentals of energy materials, Institute of Physics, Faculty of Mathematics and Natural Sciences
Technische Universität Ilmenau
98693 Ilmenau, Germany

M. A. Zare Pour, N. Mogharehabed, A. Paszuk
BMBF Junior Research Group PARASOL
Institute of Physics, Faculty of Mathematics and Natural Sciences
Technische Universität Ilmenau
98693 Ilmenau, Germany
E-mail: agnieszka.paszuk@tu-ilmenau.de

M. N. Qaisrani, J. L. Wolf, C. Dreßler
Theoretical Solid State Physics
Institute of Physics, Faculty of Mathematics and Natural Sciences
Technische Universität Ilmenau
98693 Ilmenau, Germany

C. Höhn, R. van de Krol
Institute for Solar Fuels
Helmholtz-Zentrum Berlin für Materialien und Energie GmbH
14109 Berlin, Germany

The ORCID identification number(s) for the author(s) of this article can be found under https://doi.org/10.1002/adfm.202506105

DOI: 10.1002/adfm.202506105

bandgaps, enabling the design of multi-junction configurations. In such structures, III-V photoabsorbers with different bandgaps but the same lattice constant can absorb different portions of the solar spectrum, thereby optimizing solar-to-fuel (STF) or solar-to-electricity efficiency. Devices based on III-V semiconductor multi-junction structures have consistently led in efficiency records for photovoltaic[4–8] and solar-to-fuels[9–11] conversion efficiencies. Among III-V materials, type III-phosphorus (III-P) compounds exhibit exceptional thermal stability and high electron mobility, making them highly suitable for advanced optoelectronic devices and multi-junction PV or PEC cells.[4,10–13]

The major challenge in developing PEC devices based on III-P semiconductors is surface corrosion upon contact with the aqueous electrolyte during operation. Corrosion can lead to increased surface charge carrier recombination[14] or even to dissolution of the top layer and the underlying III-V photoabsorber,[15] ultimately considerably reducing the device stability. A common approach to preventing corrosion in semiconductor photoelectrodes is the deposition of a thin metal oxide layer. Titanium dioxide (TiO_2) is a promising candidate for this purpose[10,11,16,17] due to its excellent chemical stability across a wide pH and potential range.[18,19] Additionally, TiO_2 is optically transparent due to its large bandgap and exhibits good electronic conductivity. When used to protect a p-type III-V photoabsorber, the TiO_2 selectively extracts the minority charge carriers from the conduction band of the underlying III-V material, while the majority carriers (holes) are blocked due to the large valence band offset. This charge carrier-selective behavior helps to maintain a high photovoltage.[10,11,17,20] To achieve high solar-to-hydrogen efficiencies, the photovoltage must be maximized by minimizing, or ideally avoiding, charge carrier recombination at the heterointerfaces.[1] In addition, detrimental Fermi level pinning effects by interfacial midgap surface/interface states must be avoided to secure preferential contact properties. The surface preparation of III-P semiconductors prior to TiO_2 deposition affects not only the surface properties such as presence of an electron trapping surface states[21] but also interaction with precursors such as water or oxygen,[22–24] which are commonly used in the deposition of TiO_2 in atomic layer deposition (ALD) processes. Thus, defect states in the bandgap have an effect on both the band alignment and the position of the Fermi level, which impacts the photovoltage as well as non-radiative charge carrier recombination, reducing the photocurrent, the voltage, and possibly the formation of chemically reactive surface bonding sites, which may lead to corrosion.

P-type indium phosphide (InP) is one of the most efficient photocathode materials available for solar water splitting and has been extensively studied.[25–28] Combining p-type InP photoabsorbers with TiO_2 results in improved photovoltage generation.[17,20,29–31] InP-based ternary compounds, such as AlInP or GaInP, are commonly used as p-n photoabsorbers or thin n-type charge carrier-selective contacts in multi-junction devices, which hold world records for solar-to-electricity and solar-to-hydrogen efficiencies.[4,10] Various surface treatment methods of InP(100) surfaces, including electrochemical etching[32] or photoelectrochemical conditioning, have been extensively studied to reduce the native oxide layer and form a well-defined one that can also passivate the surface.[27] Such passivation procedures can be adapted to more complex ternary III-P compounds, leading to a controlled Fermi level shift and improved band alignment between the formed oxide and III-V semiconductor.[11,14]

An alternative to chemical etching of the native oxide is thermal deoxidation, for example by annealing the substrates in the metalorganic vapor-phase epitaxy (MOVPE) reactor.[33] Under H-based ambient conditions, the surface reconstruction of InP(100) is dictated by the phosphorus chemical potential, which can be controlled by adjusting the precursor molar flow rate and substrate temperature. Two distinct surface reconstructions can be prepared: (i) the P-rich surface: a phosphorus terminated surface with $(2 \times 2)/c(2 \times 4)$ reconstruction consisting of buckled P–P dimers, each stabilized by one hydrogen atom,[33,34] and (ii) the In-rich surface: with (2×4) reconstruction, terminated by a mixed In–P dimer.[35] The interaction of water and oxygen with these two surfaces has been extensively studied through experimental investigations as well as theoretical calculations. The surface reconstruction of InP(100) plays a critical role in the formation of chemical species, which in turn significantly impacts surface stability.[23] While In-rich surfaces are more reactive to oxygen than to water, P-rich surfaces are more destabilized by water than by oxygen. In–O–P bonds dominate on both surfaces after exposure to water and oxygen, whereas In–O–In bonds form more preferentially under oxygen exposure on the In-rich surface.[21,23,24,36] On P-rich surfaces, experimental observations show that, in addition to In–O–P bond formation, the topmost P–P dimers break, allowing oxygen to incorporate into the surface and form P–O–P bonds.[23]

Recent density functional theory (DFT) studies extend beyond calculating the surface structure upon contact with oxygen or water to include interactions with TiO_2. Cipriano et al. microscopically studied the heterointerface between the anatase TiO_2 films and InP(110) finding a type-II band alignment regardless of film thickness or TiO_2 surface orientation. However, direct comparison to experiments has been challenging since only amorphous TiO_2/InP heterointerfaces have been studied experimentally, with reports indicating both type-II[17] and type-I[20] alignments depending on the heterointerface preparation. In a recent publication,[37] we extracted ten geometries from the

J. Velazquez Rojas, R. van de Krol
Institute of Chemistry
Technische Universität Berlin
10623 Berlin, Germany

W. Jaegermann
Surface Science Laboratory
Department of Materials- and Geosciences
Technische Universität Darmstadt
64287 Darmstadt, Germany

E. Runge
Theoretical Physics I, Institute of Physics
Faculty of Mathematics and Natural Sciences
Technische Universität Ilmenau
98693 Ilmenau, Germany

E. Runge, T. Hannappel, C. Dreßler
Institute of Micro- und Nanotechnologies
Technische Universität Ilmenau
98693 Ilmenau, Germany

amorphous TiO_2/InP heterointerface trajectory and calculated their band alignments; while the overall alignment tends to remain type-I, the conduction band offset nearly vanishes in some configurations, suggesting that both type-I and type-II alignments may be achievable depending on the precise heterointerface structure.

A common technique for depositing TiO_2 on semiconductors is ALD. In our vapor-phase deposition procedure, ultrathin films are grown through repeated alternating half-cycles. The ALD process of TiO_2 has been extensively applied, involving various titanium (Ti) or oxygen (O) precursors as well as different substrate materials.[38,39] The three most common Ti precursors used for surface passivation on semiconductors are titanium tetrachloride ($TiCl_4$),[40–42] titanium tetraisopropoxide (TTIP),[38,39] and tetrakis(dimethylamino)titanium (TDMAT).[17,38] TiO_2 grown from $TiCl_4$ and (H_2O) has demonstrated enhanced performance for Si surface passivation and as an electron-selective contact.[43] While the ALD reaction steps of TiO_2 using these precursors has been extensively studied on Si,[41–44] research on InP substrates remains limited and has primarily focused on bulk TiO_2 properties.[17,20,38,39] However, a detailed investigation of the chemical composition of the InP substrate during the initial stages of ALD, as well as of the formation of the heterointerface and the evolution of band alignment throughout the different growth stages are still mostly missing. Substrate surface reactions and the potential formation of different oxide species during the initial stages of TiO_2 nucleation and growth can result in a highly complex heterointerface which can impact interfacial charge carrier injection, transport, and recombination. Furthermore, depending on the Ti precursor, atomic impurities can absorb onto the semiconductor substrate, introducing electronically active states within the band gap. For a fundamental microscopic understanding of the surface and heterointerface chemistry, contamination-free and atomically well-defined surfaces are essential. Without such well-defined surface studies, it is difficult to resolve the heterointerface properties experimentally, and it becomes more difficult to simulate more complex surfaces for theoretical comparisons.

Hence, we have investigated the chemical composition and the band alignment of the amorphous TiO_2/InP heterojunction. We combine (DFT-based) ab initio molecular dynamics (AIMD) calculations with experimental results based on ultraviolet photoemission spectroscopy (UPS) and X-ray photoemission spectroscopy (XPS) during the initial nucleation process and growth of TiO_2 from $TiCl_4$ and H_2O on P-rich InP(100) substrates. We have analyzed the changes in the elemental composition and chemical state of the P-rich InP(100) surface after the very first ALD cycles and after subsequent growth of very thin TiO_2 layers. The transfer from the ALD chamber to the XPS chamber was performed in ultrahigh vacuum (UHV) conditions to avoid any surface contamination. Therefore, our systematic, contamination-free study provides a comprehensive atomic-scale understanding of heterointerface chemistry and band alignment. These findings contribute to the optimization of TiO_2/InP heterojunctions. Additionally, it has been shown that the dimerized P-rich InP surfaces closely resemble those of III-P.[22,45,46] Therefore, the results may also be relevant for more complex TiO_2/ternary InP-based heterointerfaces, commonly used in high-efficiency devices, including PEC systems with highest performance.

2. Results and Discussion

2.1. Chemical Composition at the Heterointerfaces Based on the Photoemission Spectroscopy

The specific ALD cycles after which XPS measurements were performed (see Atomic Layer Deposition in Experimental Section) were carefully selected to systematically investigate the chemical and electronic properties at different stages of TiO_2 growth on the P-rich InP(100) surface. These stages include: (a) modification of the P-rich InP substrate during the initial nucleation stage, (b) formation of the heterointerface, (c) the buried interface, which lies beneath the TiO_2 film and does not undergo significant changes with further TiO_2 deposition, and (d) the TiO_2 film.

Figure 1 shows XP spectra of O 1s (a), Ti 2p (b), In $3d_{5/2}$ (c), P 2p (d), and Cl 2p (e) on the P-rich InP(100) surface prior to the ALD process (black line) and after a selected number of ALD cycles. The measurement was performed at normal emission angle (90°). Prior to TiO_2 deposition, no oxygen (Figure 1 a) was detected (see Figure S1, Supporting Information). Furthermore, as shown in Figure S1 (Supporting Information), no carbon contamination was observed prior to and throughout the ALD process, proving the quality of the sample transfer process. With an increasing number of ALD cycles, the intensity of the O 1s (a) and Ti 2p (b) peaks increases due to the growth of the TiO_2 film, while the emission intensity related to the InP substrate, In $3d_{5/2}$ (c) and P 2p (d) are reduced. After 212 ALD cycles, the intensities of the In $3d_{5/2}$ and P 2p core-levels approach zero. This is due to the limited information depth defined by the inelastic mean free path (IMFP) of photoelectrons, which is approximately 3×IMFPs. Given the fixed photoelectron energy of an Al *Kα* source, the IMFP reaches approximately 2.6 nm, which agrees well with the measured thickness by in situ ellipsometry (see Atomic Layer Deposition in Experimental Section).

In the initial ALD cycles, the In $3d_{5/2}$ and P 2p core-level spectra exhibit a consistent shift of approximately 100–200 meV toward higher binding energies. Although this shift is below the energy resolution of our setup (0.580 eV) and should therefore be interpreted cautiously, the fact that both core-levels shift by a similar magnitude could suggest a small variation of the valence band maximum (VBM), as discussed in the following section. This variation is attributed to minor changes in the surface electronic structure which results in increasing downward band bending induced by the changes on the surface upon TiO_2 growth. After approximately 17 ALD cycles, when the heterointerface is effectively buried beneath the grown layer, the binding energies of the core-levels remain nearly identical.

The broadening and asymmetry of the O 1s core-level after 17 and 32 ALD cycles indicate the presence of multiple oxygen-containing components. One component corresponds to oxygen in the TiO_2 bulk, while the other one is likely associated with oxygen bonded to the InP(100) surface. The energy range of the Ti 2p core-levels overlaps with the energy of the In 3d plasmons, as shown in Figure 1b. Furthermore, the photoionization cross-section of Ti 2p is around three times smaller than that of In 3d, which means that its contribution to the spectra is three times weaker, which in addition to the overlapping with the In 3d plasmons further hinders the analysis of the Ti 2p core-level.

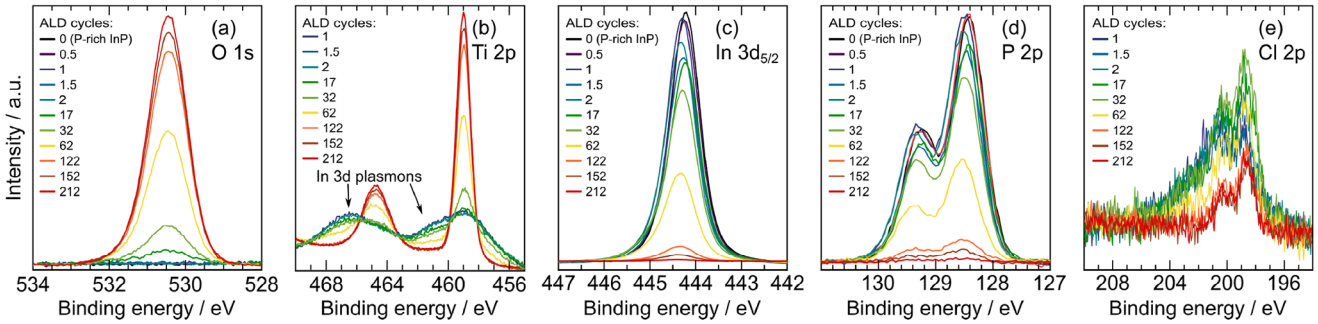

Figure 1. XP spectra of O 1s, Ti 2p, In $3d_{5/2}$, P 2p, and Cl 2p for as received sample and after 0.5, 1, 1.5, 2, 17, 32, 62, 122, 152, 212 ALD cycles. The measured binding energy values are given in Table S1 (Supporting Information).

Therefore, resolving the Ti signal after the first few cycles is challenging. After 17 cycles, a change of the intensity of the In 3d plasmon is observed and a small peak at the binding energy corresponding to Ti $2p_{3/2}$ (at 458.96 eV) is visible. After 32 cycles, we can clearly see the Ti $2p_{3/2}$ peak emerging. After introducing the first $TiCl_4$ cycle, we observed a small amount of chlorine on each surface, see Figure 1e. The Cl 2p core-level overlaps with the P 2s plasmon (see fitted spectra in Figure S2a, Supporting Information, for the sample after 2 cycles). With increasing the thickness of TiO_2, the intensity of the Cl 2p peak gradually decreases as the contribution of the P 2s plasmon decreases. After 122 cycles, at which the intensity of P 2p is close to zero, the contribution of the P 2s plasmon is also lost in Figure 1e. The fitting of the Cl 2p spectrum after 212 cycles, shown in Figure S2a (Supporting Information), reveals peaks that are related only to chlorine. The presence of chlorine after each measured cycle confirms the incorporation of chlorine in the heterointerface and in the formed TiO_2 film.

To analyze the chemical composition of the P-rich InP(100) surface during the nucleation of TiO_2 and at the TiO_2/InP heterointerface, the measured core-levels were analyzed by a detailed curve-fitting routine (for details see Sample Characterization with Photoemission Spectroscopy, Experimental Section). The first row in **Figure 2** shows the fitted core-level spectra of In $3d_{5/2}$ and P 2p of the P-rich InP(100) surface prior to TiO_2 deposition, and at normal emission angle (same spectra as shown in Figure 1). The P 2p core-level was fitted with two components. The larger component at 128.41 eV (light red line) is related to In−P bonds. The smaller surface component, which is shifted by 0.55 eV toward higher binding energies compared to the In−P component, is a characteristic fingerprint of well-studied P−P dimers on the reconstructed InP(100) surface (dark red line).[21,47]

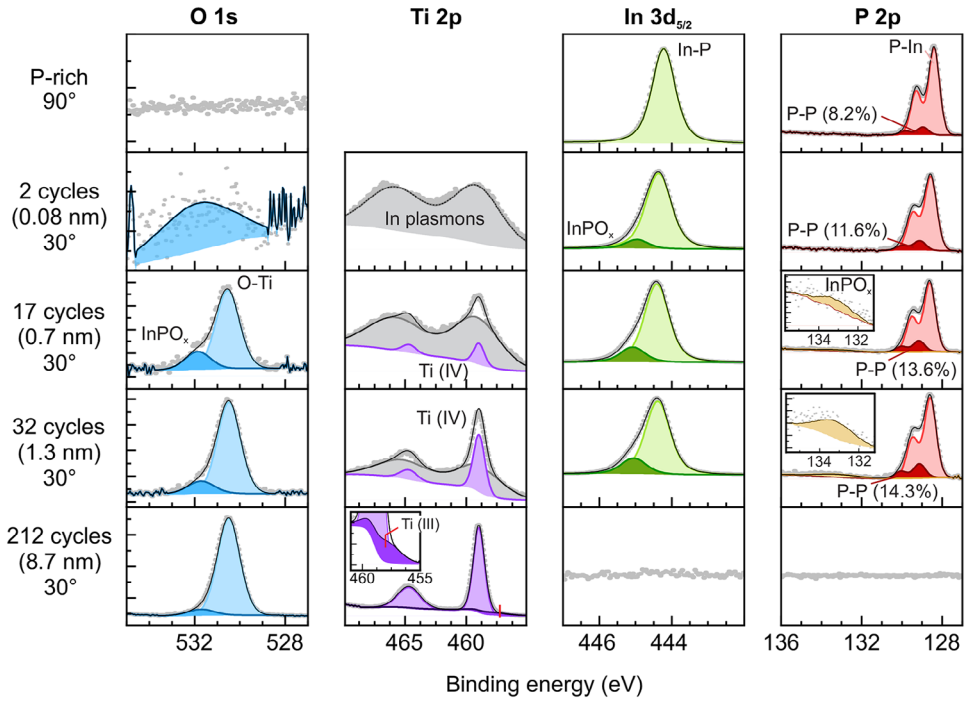

Figure 2. Fitted XP spectra of O 1s (left column), Ti 2p (second left column), In $3d_{5/2}$ (third left column), and P 2p (right column) regions of as prepared sample (top row), after 2 (second row), 17 (third row), and 212 (bottom row) ALD cycles, respectively.

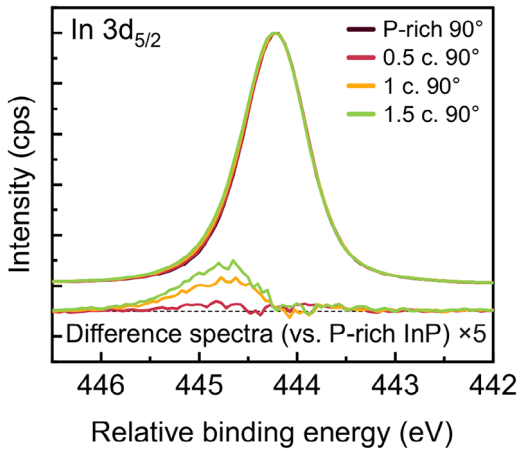

Figure 3. The XP spectra of the In $3d_{5/2}$ core-level in P-rich InP are compared after 0.5, 1, and 1.5 ALD cycles at a normal emission angle of 90°. To highlight changes in the line shapes, the difference spectra are plotted by subtracting the InP P-rich spectrum from the other spectra. To illustrate only the changes in the line shapes, peaks are shifted to maximize the overlap with P-rich InP; therefore, the x-axis represents relative binding energy.

After the first pulse of water during ALD, we did not detect the presence of oxygen in the O 1s core-level, see Figure S3 (Supporting Information). The line shape of the P 2p peak, including the region on the binding energy at which phosphates are formed (around 134 eV) did not change after the first water pulse, as shown in Figure S4 (Supporting Information). In the In $3d_{5/2}$ core-level, we observed a very small increase in signal around 444.7 eV compared to the as-prepared P-rich sample (**Figure 3**, red line). Its intensity increases with each subsequent pulse of the TiO_2 nucleation as shown in Figure 3, which compares the difference of the line-shape of the In $3d_{5/2}$ core-level before and after three first cycles. As we did not detect C, Cl or other contaminants after the first pulse of water, the small component at 444.7 eV should be related to oxygen. The contribution to the XP spectrum from the O 1s core-level is around 7.5 times weaker compared to In 3d core-level, which could explain that due to a limited resolution of our XP spectrometer we did not measure a signal of O 1s.

To enhance surface sensitivity, we performed XPS measurements in which samples were tilted 60° against normal emission (i.e., at 30° photoelectron take-off angle). After the first $TiCl_4$ pulse (1 cycle), the second water pulse (1.5 cycles), and the second $TiCl_4$ pulse (2 cycles), a similar change in the O 1s core-level was observed for all samples, see Figure S3 (Supporting Information). The fitted XP core-level spectra (measured at 30° photoelectron take-off angle) of O 1s, Ti 2p, In $3d_{5/2}$ and P 2p after 2 cycles are shown in the second row in Figure 2. In the O 1s core-level, a small increase in intensity can be observed. Although the signal is highly noisy, a rather broad peak with very low intensity can still be fitted. While one might argue that no clear feature is visible, the fitting suggests the presence of a peak with very low intensity. The broad peak in O 1s suggest more than one chemical state of oxygen, which could be associated with chemisorbed oxygen on the InP(100) surface and the initial steps in the formation of a TiO_2 film. The presence of chemisorbed oxygen on the surface after 2 cycles is confirmed by the presence of an additional peak at 445.1 eV in the In $3d_{5/2}$ core-level (dark green line), which is shifted toward higher binding energy by 0.7 eV compared to the peak related to the InP bulk (green line, at 444.4 eV). Near this binding energy, species such as $InPO_4$, $In(PO_3)_3$[48,49] and indium oxide (In_2O_3) can be expected with a higher binding energy compared to the In-P bulk by approximately 1.0–1.8 eV and 0.2–0.8 eV, respectively. Indium chloride ($InCl_x$) species are also found in this range, 0.7–1.1 eV higher than the In−P bond.[50–52] Due to the limited resolution of our XPS and the low atomic concentration of both oxygen and chlorine, we cannot confirm or rule-out the presence of any of the above-listed species, as their contribution appears as a single broad feature in the spectrum. In addition, it is reasonable to assume that at this stage of the reaction no species with well defined stoichiometry has already been formed (see also discussion below in Section 2.3)

In the P 2p core-level spectrum after 2 ALD cycles (Figure 2, second row, last column) the component related to P−P dimers remains present. This confirms that the P−P dimers in the first monolayer have not dissociated by reacting with O, Cl, or Ti. Note that the area of this component is slightly larger than the P-rich surface shown in the first row. This difference arises due to a higher surface sensitivity during the measurement, as the photoelectron take-off angle was reduced from 90° to 30°. PCl species are known to exhibit a chemical shift of 0.34 eV from the bulk InP,[53] which is only 0.2 eV lower than the binding energy of P−P dimers. If PCl species were present on the surface, their peak would overlap with the P−P dimer component. However, since no significant broadening of the surface-related peak is observed, we can exclude the presence of PCl species. Additionally, P−Ti bonds are expected to appear at 130.5 eV.[54] If present on the surface, they should be visible in the P 2p core-level spectrum, but no such feature was detected.

As the number of ALD cycles increases, XPS results (Figure 2) show the formation of characteristic TiO_2 peaks in the O 1s and Ti 2p core-levels, indicating the progressive formation of TiO_2 on the InP(100) substrate. After depositing approximately 0.7 nm of TiO_2 (after 17 cycles), the O 1s core-level intensity increases significantly, and the spectrum can be fitted with two distinct peaks (Figure 2). The larger component at 530.6 eV binding energy is related to oxygen in the TiO_2 lattice.[55] The second smaller peak at around 531.7 eV can be related to indium phosphate compounds ($InPO_x$) at the TiO_2/InP heterointerface,[23,48] as its ratio to the oxygen in the TiO_2 bulk decreases with increasing TiO_2 thickness (compare with fourth and fifth row, first column). The presence of P−O−P bonds at the heterointerface can be excluded as they are expected at 533.5 eV binding energy in O 1s core-level, which we do not observe here.[48,56,57] Indium oxide exhibits In−O−In bonds that are typically visible in the O 1s core-level at binding energies of 530.2 eV,[23,48,56] in addition to the peak in the In 3d core-level. Since this binding energy overlaps with the oxygen in the TiO_2 bulk, precise fitting is difficult. Even though we could not fit another component, we cannot exclude In−O bonds at the heterointerface.

The P 2p core-level spectra after 17 and 32 cycles, shown in Figure 2, exhibit an additional peak at 132.9 eV, confirming the formation of phosphate and phosphite species (PO_4 and PO_3) at the TiO_2/InP heterointerface.[48] Indium phosphate/phosphite compounds, $InPO_4$ and $In(PO_3)_3$, produce characteristic peaks

near the In $3d_{5/2}$, P 2p, and O 1s binding energies at 445.5, 133.9, and 531.6 eV, respectively,[48] which fits very well to our measured values, and can be assigned to the In–O–P bonds. Most probably the phosphate is already present on the surface after 2 cycles, however its detection is hardly possible due to the limited sensitivity of the XPS measurements. The area ratio of the component associated with P–P bonds, relative to the InP bulk, increases after 17 cycles and continues to rise with further TiO_2 deposition. This is due to the increasing TiO_2 layer thickness, which reduces the probed depth of the underlying InP.

The Ti 2p core-level after 17 cycles (Figure 2) shows a clear presence of Ti. The fitted gray component is related to the In 3d plasmon and its intensity decreases during further ALD growth, while the Ti 2p contribution becomes dominant. The fitting of the spectra reveals two distinct peaks at binding energies of 459.0 eV and 464.7 eV, which correspond to the Ti ($2p_{3/2}$) and Ti ($2p_{1/2}$) core-levels of Ti^{4+} cations, respectively. The intensity ratio of the $2p_{3/2}$ to $2p_{1/2}$ peaks was maintained at 2:1. We only observed a shoulder corresponding to the Ti^{3+} defects at the very last step, after 212 ALD cycles.[55] In the last row of Figure 2, a zoomed-in graph shows this contribution for the Ti 2p spectrum, in dark purple.

The O 1s core-level component at higher binding energies (ca. 531.50 eV) remains visible even after 212 ALD cycles, despite the absence of detectable In and P core-level signals. Furthermore, its relative contribution increases from 3.8% in the 90° measurement to 4.9% in the 30° measurement, suggesting that this component is primarily located at the TiO_2 surface. Considering its binding energy and the use of water as the oxygen precursor during ALD, this signal may be attributed to hydroxyl groups present on the TiO_2 surface. Additionally, the O/Ti ratio at the beginning of the ALD process is approximately 3.7 after 17 cycles and gradually approaches 2 as the TiO_2 layers grow. This suggests that at the initial stages of the ALD process the O/Ti ratio deviates from the stoichiometric value, likely due to the presence of Ti atoms additionally bonded to hydroxyl groups. As the ALD process progresses, these bonds transform into bulk-like TiO_2 bonds. Therefore the component at ca. 531.50 eV in the O 1s core-level after 17 and 32 ALD cycles stems not only from indium phosphate compounds ($InPO_4$, $In(PO_3)_3$), but also from the hydroxyl groups present on the TiO_2 surface.

Figure 4 illustrates the calculated atomic concentrations derived from fitted core-levels. The calculation method is detailed in Section 5 in the Supporting Information. Since the P 2p and In 3d core-levels contain contributions from both the InP bulk and oxide species at the heterointerface, we plotted the atomic concentrations of phosphorus and indium in the InP bulk (filled symbols) and $InPO_x$ (open symbols). Similarly, the O 1s core-level contains contributions from the oxide species at the heterointerface (open triangle symbol) as well as from the TiO_2 bulk (filled triangle symbol) and are plotted separately. However, we have not distinguished between different types of oxide species in the calculations and fitting, as their concentrations are low, and precise evaluation is beyond the resolution and surface sensitivity of the XPS results. As the thickness of the TiO_2 layers increases, the ratio of the atomic concentration of oxide species to the contributions from InP in the In and P core-levels increases, since the thickness of the probed InP layer decreases. Conversely, the ratio of InP oxide species to TiO_2 in the O 1s core-level decreases,

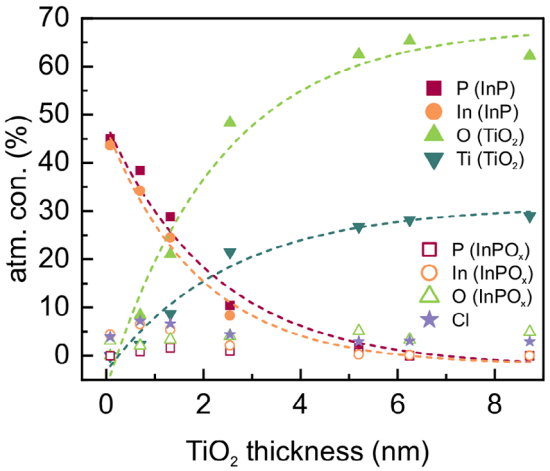

Figure 4. Calculated atomic concentration as a function of ALD cycles.

as the signal from the TiO_2 layer becomes dominant. The gradual decrease in the In and P atomic concentrations in the InP layers and the corresponding increase in O and Ti atomic concentrations in TiO_2 indicate layer-by-layer growth of TiO_2 film. Calculation of the atomic concentration of Cl shows that after 2 cycles, 4.2% Cl is present on the sample. As the number of ALD cycles increases, the Cl concentration rises to 7.2% after 17 cycles, then gradually decreases to approximately 3.0% after 122 cycles, remaining constant from that point onward. This suggests that the Cl concentration is higher at the heterointerface than in the bulk of the TiO_2 layer. However, since 3.0% of Cl remains incorporated into the sample even after 212 cycles, where the InP and the heterointerface are no longer resolvable by XPS, it indicates that a small amount of Cl is also incorporated into the TiO_2 bulk. After 212 ALD cycles, XPS measurements reveal an atomic Cl concentration of approximately 1.5% at a 90° emission angle, while at 30°, it increases to 2.9%. The higher Cl concentration observed at 30°, which is more surface-sensitive, suggests that most of the Cl is localized at the surface rather than being distributed throughout the bulk of the TiO_2 layer. Thus we conclude that the termination of the TiO_2 film consists of hydroxyl groups and chloride species. Postdeposition annealing in vacuum at temperatures above 350 °C is a well-known method to reduce the chlorine content in TiO_2 films.[41,42] Additionally, increasing the TiO_2 deposition temperature above 250 °C has also been shown to lower Cl incorporation.[58,59] However, such thermal treatments must be carefully studied, as annealing above 370 °C can lead to phosphorus desorption from the InP substrate, potentially altering the interfacial stoichiometry and electronic structure at the heterointerface.[33] While chlorine species may contribute to the observed band bending[53] their isolated effect is difficult to distinguish due to the concurrent presence of Ti and oxygen species.

To complement the XPS data, we measured the studied surfaces at different stages of TiO_2 growth using UPS. UPS is more surface sensitive than XPS and provides a significantly higher signal intensity near the valence band (VB) edge. **Figure 5** presents selected He I UP spectra of the surface before growth and after 0.5, 1, and 2 cycles (a), as well as after 17 and 212 cycles (b). The UP spectrum of the P-rich InP(100) surface (Figure 5a,b black lines) is characteristic for an atomically well-ordered

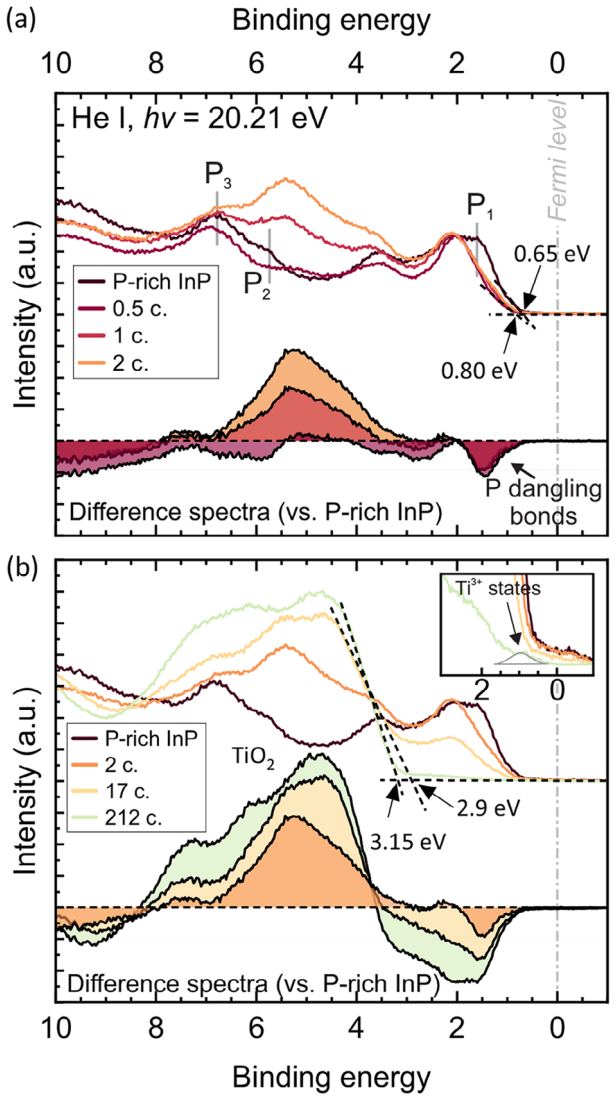

Figure 5. UP spectra of a) P-rich InP compared with the same sample after 0.5, 1, and 2 ALD cycles and b) compared with 2, 17, and 212 cycles.

surface terminated with P–P dimers.[60] A rather broad peak P_1 (1.8 eV) was assigned to a superposition of two peaks, one related to the bulk, and one closer to the VBM related to surface states. Peaks P_2 (5.8 eV) and P_3 (6.8 eV) have been associated with a surface resonance and phosphorus on the surface, respectively. Surface states (origin of the P_1 peak) were found to be introduced by a missing hydrogen atom on the P–P dimers.[21] These surface states have energy levels that lie within the bandgap and result in Fermi level pinning and band bending, as discussed in detail in Ref. [21]. Experimental and computational results showed that this H vacancy, which leaves a dangling bond defect, does not significantly change the adsorption behavior of the InP(100) surface compared to the hydrogen-saturated surface. After the first H_2O pulse, the intensity of the peak associated with the surface states reduces which indicates a reduction of the density of the dangling bond in the P–P dimers. In addition, the P_2 peak is strongly reduced, while the intensity of the P_3 peak related to the P on the surface hardly changes and other features of the spectrum remain almost identical (see red peaks in the difference of the spectra in Figure 5a). Given the high surface sensitivity of UPS, this strongly supports the XPS findings that the majority of P–P dimers remain intact on the surface. Additionally, it suggests that P–O–P bonds do not form, as the top-most P–P dimers are not dissociated by oxygen. This indicates that the surface reconstruction with some small modifications induced by the initial exposure to the ALD reactants is "buried" under the TiO_2 film. Furthermore, we observe a rise of a small peak near 5.5 eV, as shown in the difference spectrum, where the P-rich spectrum is subtracted from the spectrum after one cycle in Figure 5 (red peak). After the first water pulse is followed by the first pulse of $TiCl_4$ (1 cycle), the intensity of the peak near 5.5 eV increases significantly, while other features of the spectrum remain almost unchanged (Figure 5 light red line). The peak near 5.5 eV could be assigned to O 2p states.[23] The UP spectrum of He I after exposing the P-rich InP(100) surface to oxygen in UHV (see the Supporting Information, Section 6, Figure S5) shows a peak at same binding energy of 5.2 eV. Since no other contaminants were detected on the surface (Figure S6, Supporting Information), this peak must originate either from adsorbed oxygen or chlorine on the InP surface. This would indicate that oxygen is present on the surface already after the first water pulse. After the second cycle, the intensity of the peak near 5.5 eV further increases and no other changes in the spectrum are visible, see the difference of the spectra, orange peak in Figure 5. Since the intensity of this peak increases significantly after the first and second cycle compared to the 0.5 cycle, two additional contributions to that peak could be considered: (i) a contribution from TiO_2 species, which is expected to be small, as the XPS data suggest a very small atomic concentration of Ti; (ii) presence of Cl on the surface as the Cl 3p core-level is at 6 eV.[61,62]

The UP spectra after 17 cycles in Figure 5b provide a clear evidence of TiO_2 on the sample as a characteristic broad signal in the range of 4–8 eV is observed. Additionally, the valence band edge of TiO_2 appears around 3.2 eV. However, since the TiO_2 layer is still very thin (approximately 0.7 nm, see experimental), the VB edge of InP at lower binding energies remains visible. As the thickness of TiO_2 increases, the signal from this layer becomes more dominant, eventually at 212 cycles obscuring the InP signal, see the difference of the P-rich InP spectrum, green peaks in Figure 5b.

2.2. Empirical Band Alignment from Photoemission Spectroscopy

It was shown experimentally that TiO_2 on InP can form a type-II heterojunction,[17] while recent theoretical calculations predicted that both type-I and type-II heterojunctions are possible.[37] Based on the UPS and XPS measurements we draw the structure of the energy band alignment at the TiO_2/InP heterojunction. **Figure 6**a,b shows the energetic band alignment of bare P-rich InP and the TiO_2/InP heterointerface, respectively. The Fermi level position in the bulk of InP is estimated based on the doping concentration, where zinc acts as a p-type dopant with $N_A \approx 2 \times 10^{18}$ cm^{-3}. Using the Boltzmann approximation (k_BT) and the effective valence band density of states ($N_{VB} \approx 1.1 \times 10^{19}$ cm^{-3}),[63] the bulk Fermi level is expected to lie

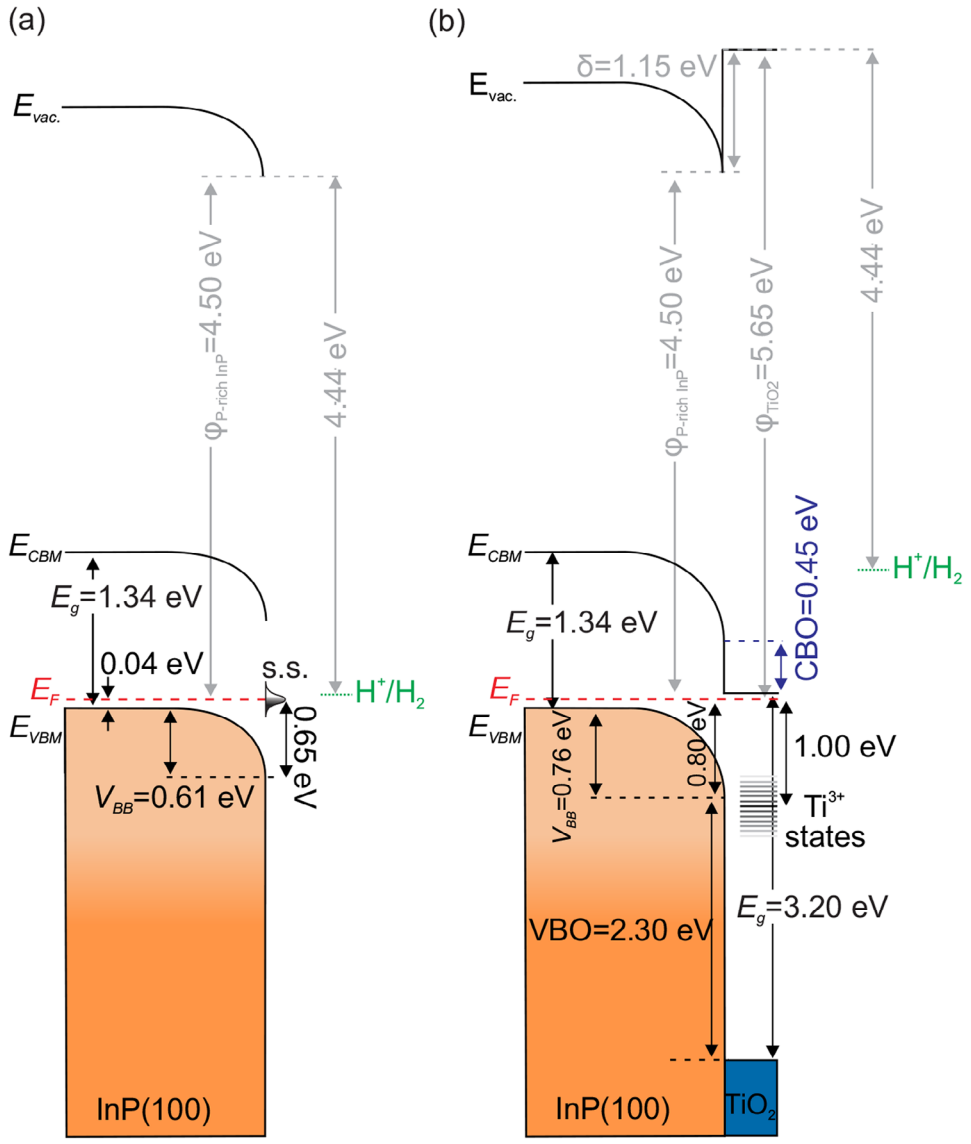

Figure 6. Band alignment of a) p-doped P-rich InP and b) TiO_2/InP heterointerface.

approximately 0.04 eV above the VBM, as calculated using Equation (1)[64]:

$$E_f - E_{VB} = k_B T \ln\left(\frac{N_A}{N_{VB}}\right) = 0.04\,eV \quad (1)$$

Figure S7 (Supporting Information) shows UPS He I spectra from all measured samples and in Figure S8 (Supporting Information), He II spectra of the initial interface formation steps are presented. In the first ALD cycles the VB of InP is dominant and as the thickness of the TiO_2 film increases, its VB is visible and the signal from the VB of InP decreases. After the first half-cycle the VBM of InP is slightly shifted toward higher binding energy, see Figure 5a. The VBM values with respect to the Fermi level (E_F - E_{VB}) on the surfaces were estimated from the intersection of the slope of each spectrum in Figure 5a,b with the extrapolated background. We estimate the VBM of the P-rich surface to 0.65 eV and the VBM of the surface after the half-cycle to 0.80 eV, see Figure 5a. To confirm whether the shift in VBM to 0.80 eV indicates an increase in band bending in InP toward the surface, we also evaluated the binding energy shift of all InP core-levels measured at 30° photoelectron take-off angle; see Table S1 (Supporting Information). The In and P core-levels, along with the InP VBM, shift toward higher binding energies by approximately 200 meV, confirming an increase in band bending in InP toward the heterointerface. The discrepancy between the measured VBM by UPS and calculated Fermi level position relative to the VBM in the bulk of InP of 0.04 eV indicates the magnitude of the surface band bending (V_{BB}) in InP. The V_{BB} is 0.61 eV for the P-rich surface and increases to 0.76 eV after the first half ALD cycle and remains constant thereafter. This change in band bending can be attributed to variations in the concentration of surface states, which influence the Fermi level pinning position, as well as the formation of new bonds and interfacial dipoles

that modify the charge carrier distribution.[65] A similar observation of an increased density of states after TiO_2 deposition on P-rich InP was previously reported using two-photon photoemission spectroscopy.[66] The flat-band condition, i.e., a rigid, step-like change in the energy diagram observed in the TiO_2 layer is consistent with the fact that the Ti $2p_{3/2}$ binding energy remains essentially unchanged across samples with different ALD cycles (see Figure S9 and Table S1, Supporting Information). This indicates negligible internal electric field in the amorphous TiO_2, which we attribute to its relatively high defect density and the high n-type doping.

After 17 cycles, the VBM of TiO_2 is estimated to be around 2.9–3.1 eV. However, precisely determining this value is challenging due to signal overlap from both TiO_2 and InP (Figure 5b, yellow line). Therefore, the VBM of TiO_2 is taken from the sample after 212 cycles, which corresponds to the TiO_2 thickness of 8.7 nm and the InP valence band is not visible anymore due to the information probe depth (~3 × IMFPs), which should be around 2.5 nm,[67] green line in Figure 5b. The UP spectrum after 212 cycles reveals mid-gap states near ca. 1 eV below the Fermi level, which is known to be related to Ti^{3+} states. These states are located in proximity to the conduction band minimum and exhibit spin-orbit splitting. One of these states, situated within the bandgap, accommodates a single electron, while the other is positioned above the conduction band minimum.[68,69] The valence band offset (VBO) is determined with two methods, based on the UPS and XPS (Kraut's approach) measurements. The difference of the VBM of InP and TiO_2 in UP spectra directly allows to determine the VBO. In Kraut's approach, the VBO is calculated by first determining the core-level binding energies relative to the VBM in the bulk material, where the heterointerface is unresolved and the crystal lattice is in its relaxed state. This gives the reference binding energies for each material. Then, the VBO is calculated by comparing the core-level binding energies of InP and TiO_2 when the heterointerface enables the determination of both values, as described in the Supporting Information. Both methods are in agreement and the VBO of ca. 2.3 eV is deduced. Considering the bandgap of 1.34 eV and 3.20 eV for InP and amorphous TiO_2, respectively, we calculated the conduction band offset (CBO) of 0.45 eV. This means the conduction band maximum (CBM) of TiO_2 is 0.45 eV below the CBM of InP and the heterostructure forms a type-II band alignment. Alvarado et al. predicted that both type-I and type-II junctions are possible for the amorphous TiO_2/P-rich InP interface, with the band alignment depending on the specific preparation conditions.[37] In our experiments we clearly observe a type-II alignment. However, variations in CBO and VBO observed in theoretical and experimental studies can be influenced by high doping concentration and the presence of mid-gap states at the heterointerface, which are challenging to accurately simulate. The downward band bending of InP toward the interface is caused by Fermi level pinning of mid-gap states related to missing hydrogen on P−P dimers.[21] Since P−P dimers are still resolved even after TiO_2 deposition, defects associated with these dimers and P dangling bonds are expected to persist. As a result, these remaining defects can still influence the band diagram and pin the Fermi level. Although the concentration of defect states within the bandgap is reduced, even a low concentration can be sufficient to induce Fermi level pinning. This is observed in our experiments as shown in the comparison of Figure 6 and also in Figure S10 (Supporting Information) indicating that the band bending induced by these surface/interface defect states is nearly not affected during the different stages of the TiO_2 over-layer growth.

Figure S9 (Supporting Information) illustrates the work function evolution of the sample at each step of TiO_2 deposition. Initially, the P-rich InP surface exhibits a work function of approximately 4.50 eV, which slightly increases after the first three half-cycles. Following two ALD cycles, the work function rises to about 5.65 eV and remains at this elevated level throughout the subsequent ALD process. Studies have shown that surface treatments can significantly influence the work function of TiO_2, with variations up to 1 eV depending on the surface condition.[70] This significant increase in work function may be attributed to the presence of chlorine anions on the TiO_2 surface, as negatively charged adsorbates can induce surface dipoles that elevate the work function.[71,72]

The band energy diagram, as it was deduced from our experimental studies, may now be related to the application of such heterointerfaces in photoelectrochemical cells. At first, one may consider the contact potential of the buried interface. Due to the existence of the electronic defect states and the band bending, the photovoltage needed for optimized conversion efficiencies which should be close to the bandgap of 1.34 eV for the InP semiconductor would be strongly reduced. This limitation has also been observed for InP photoelectrochemical cells which do not lead to sufficiently high photovoltages.[73,74] Therefore, there is a need for the preparation of heterointerfaces with lower interfacial defect concentrations which may be hard to realize. Another factor is the experimentally determined position of the work function of the TiO_2 layer which with the measured value of 5.65 eV is located at a too high positive electrode potential for H_2 evolution referred to the normal hydrogen electrode with a work function value of around 4.44 eV[75] see Figure 6b. However, when the device is in contact with an electrolyte under operational conditions and illumination, the electronic structure at the interface can change significantly. The electrode potential for H_2 evolution must be considered with care as small amounts of adsorbates from the electrolyte can significantly shift the ionization potential. Consequently, the exact position of the electrode's electronic states relative to the electrolyte's redox potentials, as deduced from the reference values without contact formation, may be shifted due to additional electrochemical dipolar potentials drops.

Under these operational conditions, the band bending in InP decreases under flat-band conditions due to the generated photovoltage.[76–78] Consequently, the conduction band position of TiO_2 shifts upward, leading to a reduction in the work function of the TiO_2 surface. Furthermore, operational conditions may facilitate the removal of chloride species, which act as negatively charged adsorbates, thereby further elevating the conduction band position of TiO_2. Ultimately, this shift may position the conduction band of TiO_2 above the reduction potential of water, a crucial requirement for the cathodic side in water-splitting PEC devices. For a more detailed analysis of the energetic conditions under operational conditions, additional series of experiments using near ambient-pressure XPS set-ups working with wet electrolyte contacts are required[79,80] and are planned for the future. Furthermore, as the chemical composition at the (buried)heterointerfaces is rather complex, using synchrotron

radiation with higher sensitivity and resolution may be needed to get a more detailed insight of the interfacial reactions and electronic structure.

2.3. Discussion of the Experimental Part

To summarize the experimental part based on the analysis of the XPS and UPS measurements, we suggest that the hydrogen terminated P−P dimer is not a favorable bonding site for water, as the molecule preferably sits in the trench between the P dimer rows, which agrees with previous theoretical and experimental analysis.[21] As a consequence, also the initial adsorption and dissociation of the precursor molecules of the ALD process seems to be hindered by unfavorable bonding sites. This leads to an initiation sequence without deposition of TiO_2. The initial nucleation of TiO_2 on the P-rich InP(100) surface at 200 °C appears to induce surface changes similar to those observed by May et al. after prolonged exposure to either water or oxygen at room temperature.[23] They reported that oxygen attacks the bond between the first-layer P atom and the second-layer In atom. However, in contrast to their findings, we did not observe P−O−P species formed by breaking of P−P dimers in the top layer, which may be due to the significantly shorter exposure time. After exposure to water and oxygen, the P-terminated ternary surface of GaInP(100) show that the P−P dimers remain on the surface.[22] While we can confirm the the presence of In−O−P species on the surface, we cannot exclude hole-trapping In−O−In bonds, but if present, their atomic concentration is rather low, based on the analysis of the core-levels of In $3d_{5/2}$ and O 1s. Ti does not bond to P, but to O placed in the second monolayer. This is probably also the reason that $TiCl_4$ does not dissociate initially on the P-terminated surface as also In−Ti bonds are not easily formed. In contrast, the formation of In−Cl bonds is preferred which may thus provide catalytic sites for the further ALD growth. The TiO_2 film grows over the P−P dimers. As a result of the complex initial deposition steps, the surface states related to the P−P dimers and in consequence the downwards band bending remains present at the heterointerface after the deposition of TiO_2. Chlorine is deposited in small amounts as chloride ion on the initial P-rich InP surface and remains present on the growing TiO_2 layer. As a result, the buried junction formed between p-doped InP and n-doped TiO_2 shows Fermi level pinning due to the still existing interface states reducing the contact potential. Additionally, the band alignment of InP to the TiO_2 and the large work function of the deposited TiO_2 layer may reduce the energetic driving force (photopotential) in the electrochemical cell for the application in H_2 evolution.

As is evident from the presented results, the formation and initial reactions steps in the deposition of passivating oxide layers, in this case TiO_2, may be rather complex. In order to gain a more detailed atomistic understanding of the buried TiO_2/InP heterointerface and to better interpret the experimental results, we performed AIMD simulations, which provide valuable insights.

2.4. Computational Results

We performed ab initio molecular dynamics (AIMD) simulations to obtain a detailed atomistic picture of the TiO_2/InP interface.

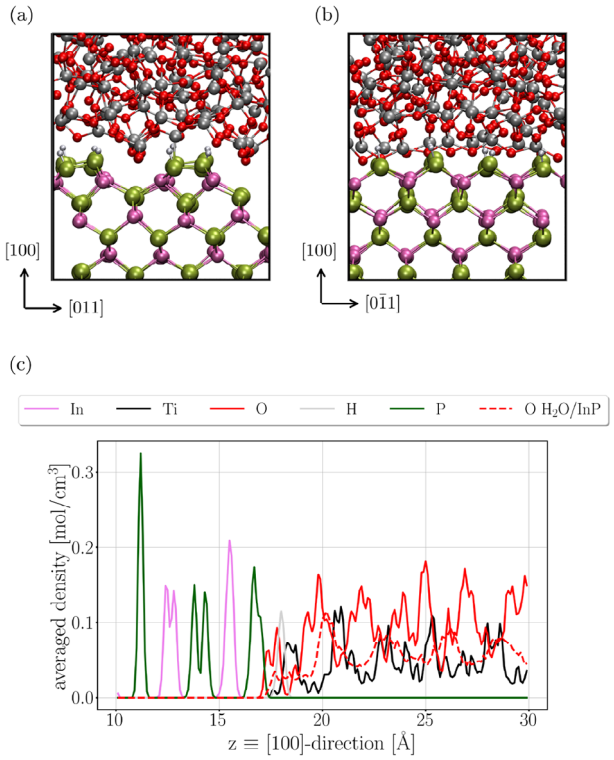

Figure 7. Subfigures (a) and (b) show snapshots from an AIMD simulation of the TiO_2/InP interface. For these simulations perfect surface terminations are assumed consisting of H terminated P-P dimer passivated InP. In (a), oxygen atoms are observed to populate the trenches, while (b) demonstrates the short-range order induced by the InP surface–characterized by alternating layers of Ti and O atoms. Subfigure (c) presents the atomic density distributions along the [100] *equiv* z-axis for the TiO_2/InP interface. For comparison, the oxygen density for the H_2O/InP interface is shown as a dashed line. **Color scheme**: O: red; H: light grey; P: green; In: violet; Ti: dark grey/black.

For these simulations perfect surface terminations are assumed which consist of H terminated P−P dimer passivated InP(100) surfaces. Analysis of the AIMD trajectories allowed us to compute interatomic distances and elucidate the bonding patterns between atoms at each time step. To assess whether oxygen species on the InP surface behave uniformly, we also carried out AIMD simulations of the technologically relevant H_2O/InP interface for comparison.

First, we report that the surface reconstruction - particularly the P-dimers - remains intact throughout the AIMD simulation timescale, consistent with experimental findings. Originally present small concentrations of missing H atoms on the P-P dimers are not considered in the simulation; also the initially formed reactive interface is not yet taken into account.

Figure 7 presents snapshots from the trajectory of the TiO_2/InP system. These snapshots reveal that oxygen atoms occupy the trenches in the InP surface reconstruction and that a short-range order - characterized by alternating layers of Ti and O atoms - is present near the InP surface.

However, a reliable description of the atomic structure can only be achieved by averaging over the entire MD trajectory. Accordingly, we computed atomic density profiles (see Figure 7c) along

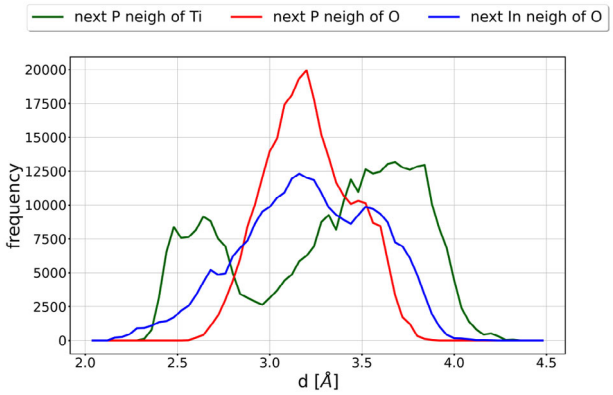

Figure 8. Histogram of distances between Ti or O atoms located near the InP surface and their nearest P or In neighbors.

the [100] direction (perpendicular direction to the InP surface). From Figure 7c we derive that (1) the atomic densities of P and O atoms overlap, and (2) the densities of O and Ti atoms near the InP surface exhibit distinct minima and maxima. These findings confirm that (1) oxygen atoms not only fill the surface trenches but also (2) contribute to the formation of the surface-induced short-range order.

Figure S11 (Supporting Information) shows the radial distribution functions (RDFs) for the P–O, In–O, and Ti–P distances, confirming the presence of very short interatomic distances corresponding to covalent bonds.

Figure 8 presents the distances between Ti or O atoms located near the InP surface and their nearest P or In neighbors. "Proximity to the InP surface" is operationally defined by selecting meaningful maximum z-values in Figure 7c: z <18.5 Å for O and $z < 20$ Å for Ti. We observe that many of the nearest P or In neighbors are more than 3 Å away from the Ti or O atoms, indicating that not every Ti or O atom on the InP surface forms a covalent bond with In or P atoms. Moreover, Figure 8 clearly shows that In–O distances are much smaller than P–O distances, suggesting a preferential interaction between In and O atoms.

In the Supporting Information, Figure S12 illustrates the distances between Ti or O atoms near the InP surface and their next-nearest P or In neighbors. The distance distribution confirms that none of these contacts is shorter than 3.0 Å. This finding indicates that covalent bonds are not formed between these atoms, thereby ruling out the formation of (symmetric) P–O–P and In–O–In bonds.

For a quantitative understanding of the bonding pattern at the interface, **Table 1** reports the average minimum distances for P–O, In–O, and Ti–P interactions, along with the corresponding number of bonds. In our analysis, a bond is defined as any pair of atoms with a distance less than 2.7 Å for P–O and In–O interactions, and less than 3.0 Å for Ti–P interactions. It is important to note that, while we have excluded the existence of P–O–P and In–O–In bonds, this does not contradict the observation of individual P–O or In–O bonds. For example, forming a P–O–P bond would require two short O–P distances connecting one oxygen atom with two phosphorus atoms, yet our simulation reveal only one short O–P distance per oxygen atom. The minimum observed In–O or P–Ti distance is shorter than the minimum observed O–P distance, underscoring that oxygen interacts preferentially with In atoms.

The overall bonding pattern at the surface and the resulting short-range order can be attributed to the strong oxygen–indium interaction. This can confirm the experimental results, of the formation of In–O–P bonds, by oxygen atom attaching to In in the second monolayer. As implied by the snapshot of the interface shown in Figure 7b, Ti and O atoms form ...–O–Ti–O–Ti–O–... zigzag chains within the trenches of the surface reconstruction. These zigzag chains can be viewed as two parallel strands of atoms that are relatively shifted with respect to each other.

In contrast to phosphorus, indium atoms are embedded within the InP interface because they do not form dimers on the surface. To facilitate the attractive interaction between oxygen and indium atoms, oxygen preferentially populates the lower strand of the zigzag chain, which penetrates deeper into the trenches. Consequently, oxygen atoms establish a first layer or chain within the trenches. In addition to interacting with indium, the oxygen atoms form covalent bonds with titanium atoms. These titanium atoms constitute the upper strand of the zigzag chain, forming a second layer or chain within the trenches. Owing to their proximity to the phosphorus dimer atoms, these titanium atoms exhibit short Ti–P distances. The predicted formation of Ti–P covalent bonds per unit cell has a low probability; as shown in Figure 7a, only one Ti–P bond is typically identified per snapshot. If such bonds are present at the heterointerface, their concentration would be below the XPS detection limit, which could explain the absence of a P 2p peak near 130.5 eV. However, XPS confirms that oxygen atoms are bonded to the underlying monolayer beneath the P–P dimers prior to Ti detection. As the Ti atoms follow the oxygen atoms structurally, they are positioned close to the surface phosphorus atoms, supporting the geometrical proximity required for Ti–P bonding suggested by theory.

The ...–O–Ti–O–Ti–O–... zigzag chain completely fills the valley, and the upper titanium strand is further covered by an additional layer of covalently bonded oxygen atoms. This outer layer is less ordered due to the lack of confinement by the InP surface reconstruction. With increasing distance from the well-ordered chain in the trenches, the TiO_2 phase becomes progressively more amorphous or less ordered.

To compare the bonding patterns of oxygen atoms at the InP surface for different oxygen-containing compounds, we performed AIMD simulations of the H_2O/InP interface. Consistent with previous AIMD simulations,[36,81] we observed that the P-dimers remain intact throughout the simulation. Instead of forming bonds with the P-dimers, the oxygen atoms of the water

Table 1. Time average of a) the minimum P–O, In–O, and Ti–P distances, and b) the number of bonds formed per simulated system size.

	TiO_2/InP	H_2O/InP
min. P - Ti distance [Å]	2.46	–
min. In - O distance [Å]	2.56	2.73
min. P - O distance [Å]	2.76	3.05
no. of Ti-P atoms < 3.0 Å	3.57	–
no. of In - O atoms < 2.8 Å	1.67	0.82
no. of P - O atoms < 2.8 Å	0.98	0.0

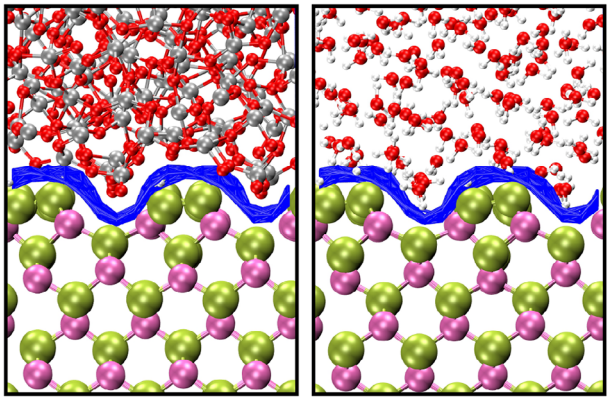

Figure 9. Snapshots from AIMD simulations of the H_2O/InP (right) and TiO_2/InP (left) interfaces. Willard–Chandler interfaces (blue) are obtained from all atoms in the InP phase. Oxygen atoms in the TiO_2 system penetrate much deeper into the trenches of the InP surface reconstruction compared to those in the H_2O system. **Color scheme**: Oxygen: red; Hydrogen: light grey; Phosphorus: green; Indium: violet; Titanium: dark grey.

molecules also tend to occupy the trenches of the surface reconstruction. In **Figure 9**, we compare snapshots of the H_2O/InP and TiO_2/InP interfaces. Willard–Chandler interfaces (WCIs) were calculated for these snapshots. WCIs represent planes of constant atomic density and can be used to define the surface of a compound in heterogeneous systems.[82] In this study, WCIs were determined from the positions of all atoms in the InP phase. By comparing the distances of oxygen atoms to the WCIs in Figure 9, we observe that oxygen atoms in the TiO_2 system penetrate much deeper into the trenches of the InP surface reconstruction compared to those in the H_2O system. This reduced penetration depth of the water oxygen atoms is also confirmed by the density profiles in Figure 7c, where the dashed line represents the oxygen density from H_2O. In line with the interpretation of the snapshots, we find that the smallest observed O–P distance in the H_2O/InP system is significantly larger than that in the TiO_2/InP system (3.05 Å vs 2.76 Å, cf. Table 1)

MD simulations indicate that the amorphous TiO_2/InP interface exhibits short-range order - characterized by alternating layers of Ti and O atoms. Oxygen atoms preferentially interact with In rather than P atoms, tending to occupy the trenches of the surface reconstruction. This tendency is significantly more pronounced in the TiO_2 system compared to the water system. Consistent with the XPS measurements, we observe that P−P dimers remain intact on the surface and that P−O−P bonds do not form, as the topmost P−P dimers are not disrupted by oxygen. Furthermore, our calculations provide no evidence for the formation of In−O−In bonds. The atomically well-ordered P-rich InP(100) surface induces an ordered arrangement of oxygen on the InP(100) surface and a subsequent ordered arrangement of Ti at the heterointerface. This initial ordering further guides the growth of TiO_2, resulting in a crystalline structure within the first few monolayers before transitioning to an amorphous bulk. The experimentally observed small concentrations of interfacial defects either due to not H-passivated P−P dimers or due to the initially formed interfacial nucleation sites of the ALD process will not be further changed when the ALD deposition of TiO_2 set in.

3. Conclusion

We have systematically studied the chemical composition and electronic structure of the TiO_2/InP(100) heterointerface using a combined experimental and theoretical approach. Our XPS and UPS measurements, complemented by AIMD simulations, reveal that the P-terminated InP(100) surface retains the existing P−P dimers during the initial ALD cycles. But the selective binding of O with In in the second substrate monolayer and P in the first monolayer leads to the formation of $InPO_x$ species to which Ti atoms are bonded. Both experimental and theoretical results provide no evidence for the formation of In−O−In and P−O−P bonds. We confirm the presence of residual chloride ions from the $TiCl_4$ precursor on InP and TiO_2 surfaces. The atomically ordered P-rich InP(100) surface induces a structured oxygen arrangement, guiding the initial growth of TiO_2 in a crystalline manner before transitioning to an amorphous phase. The band alignment analysis confirms a type-II heterojunction, with a conduction band offset of 0.45 eV, which facilitates charge carrier separation crucial for photoelectrochemical applications. However, small amounts of the initial concentrations of surface defects resulting from missing H-passivation of some of the P−P dimers predominate and are not passivated by the growing TiO_2 passivation layer. Additionally, the initial nucleation of the TiO_x overlayer leads to the formation of interfacial defects to chemisorbed chloride and oxide. These interfacial defects lead to Fermi level pinning reducing the operative band bending at the n-TiO_2/p-InP heterojunction. These insights into interfacial chemistry and band alignment are instrumental in optimizing charge carrier transport in semiconductor-based energy conversion devices. To mitigate the observed downward band bending, future studies could explore alternative Ti and O precursors, modified ALD process parameters, group-III-rich (Al)InP(100) surface terminations, or surface modifications such as the controlled formation of specific oxygen-containing species, such as phosphates. The findings presented here contribute to the broader understanding of metal oxide/III-V heterointerfaces and serve as a foundation for future engineering strategies to advance photoelectrochemical applications.

4. Experimental Section

Experimental Part—Sample Preparation: P-rich (2 × 1)-like InP(100) surfaces were prepared using a horizontal-flow MOVPE reactor (Aixtron, AIX-200) on p-doped InP(100) substrates. The substrates had a doping concentration of 2×10^{18} cm^{-3} (Zn-doped) and a 0.1° miscut toward the [111] direction. Before surface preparation, the InP(100) wafers were deoxidized at 620 °C for 10 minutes by supplying tertbutylphosphine (TBP) as a precursor, with H_2 used as a carrier gas.[83] Following deoxidation, a 100 nm thick homoepitaxial layer was grown at 600 °C, using TBP, trimethylindium (TMIn), and diethylzinc (DEZn) as the p-dopant precursor. After the growth, the samples were cooled under a TBP precursor to prepare a dimerized P-rich surface applying a well-established process procedure described in literature.[60,83,84] On multiple samples, changes in atomic ordering were monitored throughout each preparation process using in situ reflection anisotropy spectroscopy (RAS), an optical method highly sensitive to the asymmetrically reconstructed (100) surfaces of cubic crystals.[85] The RAS measurements (LayTec EpiRAS-200) were aligned to detect differences in reflection along the [0$\bar{1}$1] and [011] directions and provided a characteristic spectral fingerprint indicative of the P-rich termination and (2 × 2)/c(2 × 4) reconstruction (see Figure S13, Supporting

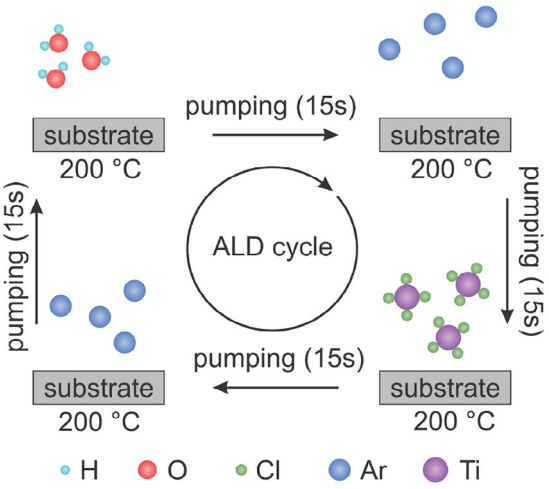

Figure 10. Schematic of an ALD cycle.

Information). Such RA spectrum was previously benchmarked with scanning tunneling microscopy in which P–P dimers were resolved.[86] The prepared P-rich InP(100) samples were transferred from the MOVPE reactor to UHV-based characterization techniques using a mobile UHV shuttle with a base pressure of $\leqslant 5 \times 10^{-10}$ mbar.[87] Prior to ALD, low energy electron diffraction (LEED) was measured, shown in the Supporting Information in Figure S13, which showed the characteristic (2 × 1)-like LEED pattern with high contrast between background and spots, confirming a uniform long-range surface reconstruction.

Experimental Part—Atomic Layer Deposition: Surface modification of the P-rich InP(100) surface was conducted using ALD, a gas-phase technique for depositing ultra thin films in sub-monolayer increments through alternating half-cycles. TiO_2 thin films were deposited on the P-rich InP(100) samples using a custom-designed, hot-wall stainless steel ALD reactor. This reactor operates in line with an UHV chamber, allowing in system XPS measurements for analyzing elemental composition and chemical states during the growth process. The system, equipped with a turbo molecular pump backed by a roughing pump, achieved a base pressure of $2 - 4 \times 10^{-7}$ mbar. $TiCl_4$ (99.999%, Sigma-Aldrich) and H_2O were used as titanium and oxygen precursors, respectively, both maintained at room temperature. The precursors were introduced alternately via ALD diaphragm valves using a vapor-draw method without a carrier gas. The reactor wall was heated to 125 °C, while the tubing and fittings were unheated. The substrate temperature was consistently held at 200 °C during deposition.

Each precursor exposure was followed by a pump/purge/pump sequence to maintain the base pressure at $3 - 5 \times 10^{-6}$ mbar. This sequence included 15 s of pumping, a 100 ms Ar purge, and another 15 s of pumping. After 15 s pumping the base pressure is $<10^{-5}$ mbar and the mean free path becomes significantly larger than the geometry of the reactor. This ensures that gas phase reactions are effectively avoided. After completing each deposition cycle, an additional H_2O pulse/purge sequence was performed. For experiments evaluating the ALD process's impact, the $TiCl_4$ pulse and purge steps were omitted while keeping the rest of the procedure unchanged. **Figure 10** depicts the schematic of a ALD cycle. **Table 2** presents the number of ALD cycles and corresponding TiO_2 thickness which was measured by ellipsometry (see Figure S14, Supporting Information). The thickness was measured in situ by spectroscopic ellipsometry (J.A. Woollam Co. Inc., M-2000D, 193-1000 nm). The dielectric function of the TiO_2 films was modeled with a Tauc-Lorentz dispersion formula.[88] The TiO_2-growth per cycle is found to be 0.04 nm per cycle.

Experimental Part—Sample Characterization With Photoemission Spectroscopy: Spectroscopy XPS characterization was performed using a SPECS Focus 500 monochromator and a Phoibos 100 electron analyzer, employing Al *Kα* radiation (1486.74 eV). The XP spectra were collected at a 90° photoelectron take-off angle, with the X-ray source and analyzer separated by an angle of 54.7°. High-resolution core-level peaks were recorded with a pass energy of 10 eV, step of 0.05 eV, and energy resolution of 0.580 eV (verified by measuring the full width at half maxima (FWHM) of Ag 3d core-level). The fitting of the XP core-level spectra were done using software CASA XPS. A Shirley background was used for all core-levels except In $3d_{5/2}$ for which a Tougaard background was used. For P 2p and O 1s a Gaussian/Lorentzian line shape was used, for Ti 2p and In $3d_{5/2}$ a Voigt function was used. An asymmetry in the In $3d_{5/2}$ core-level was considered. The P 2p and Ti 2p core-levels were fitted with the spin-orbit splitting with the ratio of $2p_{3/2}$ and $2p_{1/2}$ of 2:1. The ratio of FWHM of $2p_{3/2}$ and $2p_{1/2}$ peaks was equal for P 2p and 1:2 for Ti 2p core-levels.

Grazing incidence X-ray diffraction (GIXRD) was employed to investigate the morphology of TiO_2 layers deposited on an InP (PANalytical X'Pert Pro MPD). Measurements were conducted at grazing incidence angles (Ψ) of 1° and 3° to analyze the structural properties of the thin film, see Figure S15 Section 14 of the Supporting Information.

Computational Details—Preparation of Initial Structures for Simulation: The TiO_2/InP heterointerface was constructed by the following protocol: Starting from an InP slab, additional TiO_2 building blocks were added to the simulation box, corresponding to the rutile structure. In a second step, a classical MD simulation at 2273.15 °C (2000 K) utilizing the force field of of Matsui and Masaki[89] was used to convert the crystalline rutile structure into amorphous a-TiO_2. During the classical MD simulation, the positions of the atoms of the InP slab were fixed and the Ti and O atoms were free to move. After subsequent annealing of the system for 100 ps at –273.15 °C (0 K), the resulting structure was subjected to geometry optimization at the DFT level and used as the initial frame for an AIMD simulation. Annealing at –273.15 °C (0 K) should ensure a well-relaxed structure as the starting point for the DFT-based MD simulations. It results in only minor differences in the relaxed structures and does not critically influence the final structural model used in our DFT simulations. The classical MD simulations were performed by the program package Lammps.

Computational Details—Ab Initio Molecular Dynamics Simulation: Ab initio molecular dynamics simulations (Born-Oppenheimer MD scheme) of the a-TiO_2/InP and H_2O/InP heterointerface are performed using the CP2K program package.[90–92] The electronic structure was calculated with density functional theory using the PBE[93,94] functional. A basis set of the type DZVP-MOLOPT-SR-GTH[95] and GTH pseudopotentials[96,97] were chosen. The empirical dispersion correction (D3) of Grimme was utilized to account for van der Waals interactions.[98] The temperature is set to 19.85 °C (293 K) by a Nose-Hoover chain thermostat[99–101] (NVT ensemble). AIMD simulations are performed for 15 ps of the a-TiO_2/InP and 10 ps of the H_2O/InP and terminated the bottom of each InP slab with an indium layer and additional pseudo-hydrogen atoms to mimic the bulk properties. The positions of these indium and pseudo-hydrogen atoms were kept fixed during all simulations. The H_2O/InP [a-TiO_2/InP] system was comprised of 787 [676] atoms. For the InP surface, we used the b-(2 × 1)-H, "buckled dimer," reconstructed P-rich surface reported by Schmidt

Table 2. Number of ALD cycles and corresponding TiO_2 thickness.

# of ALD cycles	TiO_2 Thickness [nm]
0.5	(H_2O) puls
1	0.04
1.5	(H_2O) puls
2	0.08
17	0.70
32	1.32
62	2.55
122	5.20
152	6.25
212	8.72

et al.[102,103] During the AIMD simulations the P–P dimers were fully mobile.

Supporting Information

Supporting Information is available from the Wiley Online Library or from the author.

Acknowledgements

The authors gratefully acknowledge the financial support of the German Research Foundation (DFG) through project PAK 981 (project numbers HA3096/14-1 and KR4816/1-1). M.Z., N.M., and A.P. acknowledge funding from the Federal Ministry of Education and Research (BMBF) through SINATRA: PARASOL project (project number 033RC037). T. H. and M. Z. are grateful for funding from the BMBF through H2Demo project (project number 03SF0619). E.R., C.D., and T.H. also gratefully acknowledge the financial support of Carl-Zeiss-Stiftung through project SustEntMat. The authors express their gratitude to Antonio Müller for providing technical assistance throughout the series of experiments and transferring samples between institutes.

Open access funding enabled and organized by Projekt DEAL.

Conflict of Interest

The authors declare no conflict of interest.

Data Availability Statement

The data that support the findings of this study are available from the corresponding author upon reasonable request.

Keywords

ab initio molecular dynamics, atomic layer deposition, band alignment, solar to fuel conversion, TiO_2/InP heterointerface

Received: March 8, 2025
Revised: April 24, 2025
Published online:

[1] T. Hannappel, S. Shekarabi, W. Jaegermann, E. Runge, J. Hofmann, R. van de Krol, M. M. May, A. Paszuk, F. Hess, A. Bergmann, A. Bund, C. Cierpka, C. Dreßler, F. Dionigi, D. Friedrich, M. Favaro, S. Krischok, M. Kurniawan, K. Lüdge, Y. Lei, B. Roldan Cuenya, P. Schaaf, R. Schmidt-Grund, W. G. Schmidt, P. Strasser, E. Unger, M. F. Vasquez Montoya, D. Wang, H. Zhang, *Sol. RRL* **2024**, 1.
[2] F. F. Abdi, L. Han, A. H. M. Smets, M. Zeman, B. Dam, R. van de Krol, *Nat. Commun.* **2013**, *4*, 1.
[3] F. Urbain, V. Smirnov, J. P. Becker, A. Lambertz, F. Yang, J. Ziegler, B. Kaiser, W. Jaegermann, U. Rau, F. Finger, *Energy Environ. Sci.* **2016**, *9*, 145.
[4] H. Helmers, E. Lopez, O. Höhn, D. Lackner, J. Schön, M. Schauerte, M. Schachtner, F. Dimroth, A. W. Bett, *Phys. Status Solidi RRL* **2021**, *15*, 1.
[5] J. F. Geisz, R. M. France, K. L. Schulte, M. A. Steiner, A. G. Norman, H. L. Guthrey, M. R. Young, T. Song, T. Moriarty, *Nat. Energy* **2020**, *5*, 326.
[6] P. Schygulla, R. Müller, O. Höhn, M. Schachtner, D. Chojniak, A. Cordaro, S. Tabernig, B. Bläsi, A. Polman, G. Siefer, D. Lackner, F. Dimroth, *Prog. Photovolt.: Res. Appl.* **2024**, 1.
[7] National Renewable Energy Laboratory, Best research-cell efficiency chart, https://www.nrel.gov/pv/cell-efficiency.html, (accessed: 2024).
[8] M. A. Green, E. D. Dunlop, M. Yoshita, N. Kopidakis, K. Bothe, G. Siefer, D. Hinken, M. Rauer, J. Hohl-Ebinger, X. Hao, *Prog. Photovolt.: Res. Appl.* **2024**, *32*, 425.
[9] W. H. Cheng, M. H. Richter, R. Müller, M. Kelzenberg, S. Yalamanchili, P. R. Jahelka, A. N. Perry, P. C. Wu, R. Saive, F. Dimroth, B. S. Brunschwig, T. Hannappel, H. A. Atwater, *Adv. Energy Mater.* **2022**, *12*, 2201062.
[10] W. H. Cheng, M. H. Richter, M. M. May, J. Ohlmann, D. Lackner, F. Dimroth, T. Hannappel, H. A. Atwater, H. J. Lewerenz, *ACS Energy Lett.* **2018**, *3*, 1795.
[11] M. M. May, H. J. Lewerenz, D. Lackner, F. Dimroth, T. Hannappel, *Nat. Commun.* **2015**, *6*, 1.
[12] L. Meier, C. Braun, T. Hannappel, W. Schmidt, *Phys. Status Solidi B* **2021**, *258*, 2000463.
[13] F. Dimroth, M. Grave, P. Beutel, U. Fiedeler, C. Karcher, T. N. D. Tibbits, E. Oliva, G. Siefer, M. Schachtner, A. Wekkeli, A. W. Bett, R. Krause, M. Piccin, N. Blanc, C. Drazek, E. Guiot, B. Ghyselen, T. Salvetat, A. Tauzin, T. Signamarcheix, A. Dobrich, T. Hannappel, K. Schwarzburg, *Prog. Photovolt.: Res. Appl.* **2014**, *22*, 277.
[14] M. M. May, W. Jaegermann, *Curr. Opin. Electrochem.* **2022**, *34*, 100968.
[15] Y. Weilai, *Curr. Opin. Electrochem.* **2023**, *39*, 101262.
[16] C. Moon, B. Seger, P. K. Vesborg, O. Hansen, I. Chorkendorff, *Cell Rep. Phys. Sci.* **2020**, *1*, 100261.
[17] Y. Lin, R. Kapadia, J. Yang, M. Zheng, K. Chen, M. Hettick, X. Yin, C. Battaglia, I. D. Sharp, J. W. Ager, A. Javey, *J. Phys. Chem. C* **2015**, *119*, 2308.
[18] B. Seger, D. S. Tilley, T. Pedersen, P. C. K. Vesborg, O. Hansen, M. Grätzel, I. Chorkendorff, *RSC Adv.* **2013**, *3*, 25902.
[19] B. Seger, T. Pedersen, A. B. Laursen, P. C. K. Vesborg, O. Hansen, I. Chorkendorff, *J. Am. Chem. Soc.* **2013**, *135*, 1057.
[20] X. Yin, C. Battaglia, Y. Lin, K. Chen, M. Hettick, M. Zheng, C. Chen, D. Kiriya, A. Javey, *ACS Photonics* **2014**, *1*, 1245.
[21] D. C. Moritz, I. A. Ruiz Alvarado, M. A. Zare Pour, A. Paszuk, T. Frieß, E. Runge, J. P. Hofmann, T. Hannappel, W. G. Schmidt, W. Jaegermann, *ACS Appl. Mater. Interfaces* **2022**, *14*, 47255.
[22] D. Ostheimer, C. Dreßler, M. Grossmann, M. A. Zare Pour, S. Shekarabi, K. D. Hanke, J. Koch, A. Paszuk, E. Runge, T. Hannappel, *J. Phys. Chem. C* **2024**, *128*, 19559.
[23] M. May, H. J. Lewerenz, T. Hannappel, *J. Phys. Chem. C* **2014**, *118*, 19032.
[24] I. A. Ruiz Alvarado, M. Karmo, E. Runge, W. G. Schmidt, *ACS Omega* **2021**, *6*, 6297.
[25] A. Heller, B. Miller, H. J. Lewerenz, K. J. Bachmann, *J. Am. Chem. Soc.* **1980**, *102*, 6555.
[26] A. Heller, R. G. Vadimsky, *Phys. Rev. Lett.* **1981**, *46*, 1153.
[27] A. G. Muñoz, C. Heine, M. Lublow, H. W. Klemm, N. Szabó, T. Hannappel, H. J. Lewerenz, *ECS J. Solid State Sci. Technol.* **2013**, *2*, Q51.
[28] L. Gao, Y. Cui, R. H. J. Vervuurt, D. van Dam, R. P. J. van Veldhoven, J. P. Hofmann, A. A. Bol, J. E. M. Haverkort, P. H. L. Notten, E. P. A. M. Bakkers, E. J. M. Hensen, *Adv. Funct. Mater.* **2016**, *26*, 679.
[29] M. Malizia, B. Seger, I. Chorkendorff, P. C. K. Vesborg, *J. Mater. Chem. A* **2014**, *2*, 6847.
[30] Z. Xu, B. Hou, F. Zhao, Z. Cai, H. Shi, Y. Liu, C. L. Hill, D. G. Musaev, M. Mecklenburg, S. B. Cronin, T. Lian, *Nano Lett.* **2021**, *21*, 8017.
[31] S. Cao, Z. Kang, Y. Yu, J. Du, L. German, J. Li, X. Yan, X. Wang, Y. Zhang, *Adv. Energy Mater.* **2020**, *10*, 1902985.

[32] C. Kaneshiro, T. Sato, H. HidekiHasegawa, *Jpn. J. Appl. Phys.* **1999**, *38*, 1147.
[33] H. Döscher, K. Möller, T. Hannappel, *J. Cryst. Growth* **2011**, *318*, 1372.
[34] W. G. Schmidt, P. H. Hahn, F. Bechstedt, N. Esser, P. Vogt, A. Wange, W. Richter, *Phys. Rev. Lett.* **2003**, *90*, 126101.
[35] W. Schmidt, F. Bechstedt, N. Esser, M. Pristovsek, C. Schultz, W. Richter, *Phys. Rev. B:Condens. Matter Mater. Phys.* **1998**, *57*, 14596.
[36] B. C. Wood, E. Schwegler, W. I. Choi, T. Ogitsu, *J. Phys. Chem. C* **2014**, *118*, 1062.
[37] I. A. Ruiz Alvarado, C. Dreßler, W. G. Schmidt, *J. Phys.:Condens. Matter* **2024**, *37*, 075001.
[38] O. Bienek, B. Fuchs, M. Kuhl, T. Rieth, J. Kühne, L. I. Wagner, L. M. Todenhagen, L. Wolz, A. Henning, I. D. Sharp, *ACS Photonics* **2023**, *10*, 3985.
[39] O. Bienek, T. Rieth, J. Kühne, B. Fuchs, M. Kuhl, L. I. Wagner, L. M. Todenhagen, L. Wolz, A. Henning, I. D. Sharp, *Appl. Phys. Lett.* **2024**, *124*, 071601.
[40] B. Liao, B. Hoex, A. G. Aberle, D. Chi, C. S. Bhatia, *Appl. Phys. Lett.* **2014**, *104*, 253903.
[41] A. C. Bronneberg, C. Höhn, R. van de Krol, *J. Phys. Chem. C* **2017**, *121*, 5531.
[42] R. Methaapanon, S. F. Bent, *J. Phys. Chem. C* **2010**, *114*, 10498.
[43] D. Hiller, F. Munnik, J. Lopez-Vidrier, D. Solonenko, J. Reif, M. Knaut, O. Thimm, N. E. Grant, *J. Vac. Sci. Technol., A* **2024**, *42*, 032406.
[44] S. Hu, M. R. Shaner, J. A. Beardslee, M. Lichterman, B. S. Brunschwig, N. S. Lewis, *Science* **2014**, *344*, 1005.
[45] L. J. Glahn, I. A. Ruiz Alvarado, S. Neufeld, M. A. Zare Pour, P. A., D. Ostheimer, S. Shekarabi, O. Romanyuk, D. C. Moritz, J. P. Hofmann, W. Jaegermann, T. Hannappel, W. G. Schmidt, *Phys. Status Solidi B Basic Res.* **2022**, *259*, 2200308.
[46] M. A. Zare Pour, S. Shekarabi, I. A. Ruiz Alvarado, J. Diederich, Y. Gao, A. Paszuk, D. C. Moritz, W. Jaegermann, D. Friedrich, R. van de Krol, W. G. Schmidt, T. Hannappel, *Adv. Funct. Mater.* **2025**, 2423702.
[47] P. Vogt, A. M. Frisch, T. Hannappel, S. Visbeck, F. Willig, C. Jung, R. Follath, W. Braun, W. Richter, N. Esser, *Appl. Surf. Sci.* **2000**, *166*, 190.
[48] G. Chen, S. B. Visbeck, D. C. Law, R. F. Hicks, *J. Appl. Phys.* **2002**, *91*, 9362.
[49] Y. S. Lee, W. A. Anderson, *J. Appl. Phys.* **1989**, *65*, 4051.
[50] R. Chanson, S. Bouchoule, C. Cardinaud, C. Petit-Etienne, E. Cambril, A. Rhallabi, S. Guilet, E. Blanquet, *J. Vac. Sci. Technol. B* **2014**, *32*, 011219.
[51] G. E. McGuire, G. K. Schweitzer, T. A. Carlson, *Inorg. Chem.* **1973**, *12*, 2450.
[52] B. H. Freeland, J. J. Habeeb, D. G. Tuck, *Can. J. Chem.* **1977**, *55*, 1527.
[53] W. H. Hung, J. T. Hsieh, H. L. Hwang, H. Y. Hwang, C. C. Chang, *Surf. Sci.* **1998**, *418*, 46.
[54] M. A. Korotin, D. W. Boukhvalov, N. V. Gavrilov, S. S. Kim, S. O. Cholakh, E. Z. Kurmaev, *Phys. Status Solidi B* **2018**, *255*, 1700477.
[55] H. Ali-Löytty, M. Hannula, J. Saari, L. Palmolahti, B. D. Bhuskute, R. Ulkuniemi, T. Nyyssönen, K. Lahtonen, M. Valden, *ACS Appl. Mater. Interfaces* **2019**, *11*, 2758.
[56] X. Zhang, T. A. Pham, T. Ogitsu, B. C. Wood, S. Ptasinska, *J. Phys. Chem. C* **2020**, *124*, 3196.
[57] M. M. May, O. Supplie, C. Höhn, R. Van De Krol, H. J. Lewerenz, T. Hannappel, *New J. Phys.* **2013**, *15*, 1.
[58] J. Aarik, A. Aidla, H. Mändar, T. Uustare, *Appl. Surf. Sci.* **2001**, *172*, 1.
[59] C. Armstrong, L.-V. Delumeau, D. Muñoz-Rojas, A. Kursumovic, J. MacManus-Driscoll, K. P. Musselman, *Nanoscale Adv.* **2021**, *3*, 5908.
[60] T. Hannappel, L. Töben, S. Visbeck, H. J. Crawack, C. Pettenkofer, F. Willig, *Surf. Sci.* **2000**, *470*, L1.
[61] J. F. Moulder, W. F. Stickle, P. E. Sobol, K. D. Bomben, *Handbook of X-ray Photoelectron Spectroscopy*, Perkin-Elmer Corporation, Eden Prairie, MN **1992**.
[62] D. C. Moritz, Dissertation, Technische Universität Darmstadt, Darmstadt, Germany, Supervisors: Wolfram Jaegermann, Andreas Klein **2024**.
[63] M. Levinshtein, S. Rumyanstev, M. Shur, *Handbook series on Semiconductor Parameters*, Vol. *2*, World Scientific, Singapore **1999**.
[64] P. Würfel, U. Würfel, *Physics of Solar Cells: Basic Principles to Advanced Concepts*, 3rd Ed. Wiley, **2016**.
[65] R. Sciotto, I. A. Ruiz Alvarado, W. G. Schmidt, *Surfaces* **2024**, *7*, 79.
[66] J. Diederich, J. V. Rojas, A. Paszuk, M. A. Zare Pour, C. Höhn, I. A. Ruiz Alvarado, K. Schwarzburg, D. Ostheimer, R. Eichberger, W. G. Schmidt, T. Hannappel, R. van de Krol, D. Friedrich, *Adv. Funct. Mater.* **2024**, *34*, 2409455.
[67] S. Hüfner, *Photoelectron Spectroscopy: Principles and Applications*, *Advanced Texts in Physics*. Springer-Verlag Berlin Heidelberg, 3 ed., 82, **2003**.
[68] A. T. Paxton, L. Thiên-Nga, *Phys. Rev. B* **1998**, *57*, 1579.
[69] P. J. D. Lindan, N. M. Harrison, M. J. Gillan, J. A. White, *Phys. Rev. B* **1997**, *55*, 15919.
[70] S. Kashiwaya, J. Morasch, V. Streibel, T. Toupance, W. Jaegermann, A. Klein, *Surfaces* **2018**, *1*, 73.
[71] H. Onishi, A. Sasahara, *Local Work Function of Catalysts and Photoelectrodes*, Springer Berlin Heidelberg, Berlin, Heidelberg **2012**, pp. 201–219.
[72] Y. Sun, Z. Liu, P. Pianetta, *J. Vac. Sci. Technol., A* **2007**, *25*, 1351.
[73] L. Gao, Y. Cui, J. Wang, A. Cavalli, A. Standing, T. T. Vu, M. A. Verheijen, J. E. M. Haverkort, E. P. A. M. Bakkers, P. H. L. Notten, *Nano Letters* **2014**, *14*, 3715.
[74] A. Goryachev, L. Gao, R. P. J. van Veldhoven, J. E. M. Haverkort, J. P. Hofmann, E. J. M. Hensen, *Phys. Chem. Chem. Phys.* **2018**, *20*, 14242.
[75] S. Trasatti, *Pure Appl. Chem.* **1986**, *58*, 955.
[76] M. Alonso, R. Cimino, K. Horn, *Phys. Rev. Lett.* **1990**, *64*, 1947.
[77] M. G. Walter, E. L. Warren, J. R. McKone, S. W. Boettcher, Q. Mi, E. A. Santori, N. S. Lewis, *Chem. Rev.* **2010**, *110*, 6446.
[78] D. C. Moritz, W. Calvet, M. A. Zare Pour, A. Paszuk, T. Mayer, T. Hannappel, J. P. Hofmann, W. Jaegermann, *Sol. RRL* **2023**, *7*, 2201063.
[79] M. Favaro, B. Jeong, P. N. Ross, J. Yano, Z. Hussain, Z. Liu, E. J. Crumlin, *Nat. Commun.* **2016**, *7*, 12695.
[80] V. A. Saveleva, V. Papaefthimiou, M. K. Daletou, W. H. Doh, C. Ulhaq-Bouillet, M. Diebold, S. Zafeiratos, E. R. Savinova, *J. Phys. Chem. C* **2016**, *120*, 15930.
[81] B. C. Wood, E. Schwegler, W. I. Choi, T. Ogitsu, *J. Am. Chem. Soc.* **2013**, *135*, 15774.
[82] A. P. Willard, D. Chandler, *J. Phys. Chem. B* **2010**, *114*, 1954.
[83] T. Hannappel, S. Visbeck, M. Zorn, J. T. Zettler, F. Willig, *J. Cryst. Growth* **2000**, *221*, 124.
[84] T. Letzig, H. J. Schimper, T. Hannappel, F. Willig, *Phys. Rev. B: Condens. Matter Mater. Phys.* **2005**, *71*, 033308.
[85] D. E. Aspnes, A. A. Studna, *Phys. Rev. Lett.* **1985**, *54*, 1956.
[86] P. Kleinschmidt, H. Döscher, P. Vogt, T. Hannappel, *Phys. Rev. B: Condens. Matter Mater. Phys.* **2011**, *83*, 1.
[87] T. Hannappel, S. Visbeck, L. Töben, F. Willig, *Rev. Sci. Instrum.* **2004**, *75*, 1297.
[88] E. Langereis, S. B. S. Heil, H. C. M. Knoops, W. Keuning, M. C. M. van de Sanden, W. M. M. Kessels, *J. Phys. D:Appl. Phys.* **2009**, *42*, 073001.
[89] M. Matsui, M. Akaogi, *Mol. Simul.* **1991**, *6*, 239.
[90] T. D. Kühne, M. Iannuzzi, M. Del Ben, V. V. Rybkin, P. Seewald, F. Stein, T. Laino, R. Z. Khaliullin, O. Schütt, F. Schiffmann, D. Golze, J. Wilhelm, S. Chulkov, M. H. Bani-Hashemian, V. Weber, U. Borštnik,

M. Taillefumier, A. S. Jakobovits, A. Lazzaro, H. Pabst, T. Müller, R. Schade, M. Guidon, S. Andermatt, N. Holmberg, G. K. Schenter, A. Hehn, A. Bussy, F. Belleflamme, G. Tabacchi, et al., *J. Chem. Phys.* **2020**, *152*, 194103.
[91] J. VandeVondele, M. Krack, F. Mohamed, M. Parrinello, T. Chassaing, J. Hutter, *Comput. Phys. Commun.* **2005**, *167*, 103.
[92] J. VandeVondele, J. Hutter, *J. Chem. Phys.* **2003**, *118*, 4365.
[93] J. P. Perdew, K. Burke, M. Ernzerhof, *Phys. Rev. Lett.* **1996**, *77*, 3865.
[94] J. P. Perdew, K. Burke, Y. Wang, *Phys. Rev. B* **1996**, *54*, 16533.
[95] J. VandeVondele, J. Hutter, *J. Chem. Phys.* **2007**, *127*, 114105.
[96] C. Hartwigsen, S. Goedecker, J. Hutter, *Phys. Rev. B* **1998**, *58*, 3641.
[97] M. Krack, *Theor. Chem. Acc.* **2005**, *114*, 145.
[98] S. Grimme, J. Antony, S. Ehrlich, H. Krieg, *J. Chem. Phys.* **2010**, *132*, 154104.
[99] S. Nose, *J. Chem. Phys.* **1984**, *81*, 511.
[100] G. J. Martyna, M. L. Klein, M. Tuckerman, *J. Chem. Phys.* **1992**, *97*, 2635.
[101] S. Nose, *Mol. Phys.* **1970**, *52*, 255.
[102] W. G. Schmidt, P. H. Hahn, F. Bechstedt, N. Esser, P. Vogt, A. Wange, W. Richter, *Phys. Rev. Lett.* **2003**, *90*, 126101.
[103] J. Luo, J. Olson, S. R. Kurtz, D. Arent, K. Bertness, M. Raikh, E. Tsiper, *Phys. Rev. B* **1995**, *51*, 7603.